Swirling supersonic gas flow in an EIGA atomizer for metal powder production: Numerical investigation and experimental validation

Baraa Qaddah, Pierre Chapelle, Jean Pierre Bellot, Julien Jourdan, Nicolas Rimbert, Agathe Deborde, Raphael Hammes, Aurélie Franceschini

Swirling supersonic gas flow in an EIGA atomizer for metal powder production: numerical investigation and experimental validation

Baraa QADDAH[1&2&4] (baraa.qaddah@irt-m2p.fr), Pierre CHAPELLE[2], Jean Pierre BELLOT[2], Julien JOURDAN[2], Nicolas RIMBERT[3], Agathe DEBORDE[1&4], Raphael HAMMES[1&4], Aurélie FRANCESCHINI[1&4].

[1] IRT-M2P, 4 rue Augustin Fresnel, 57070 Metz, France.

[2] Institut Jean Lamour, UMR 7198 CNRS, Université de Lorraine, LabEx

DAMAS, BP 50840, 54011 Nancy Cedex, France

[3] LEMTA CNRS, Université de Lorraine, 2 Avenue de la Forêt de Haye, Vandoeuvre-lès-Nancy, 54518, Lorraine, France.

[4] MetaFensch, 109 Rue de Thionville, 57270 Uckange, France

Abstract

This paper is concerned with the modeling of the Electrode Induction Melting Gas Atomization (EIGA) process. This process employs a swirling supersonic inert gas jet to atomize a free-fall molten metal stream, with the aim to produce powders of highly reactive metals. As a first step towards the development of a complete model, this study aims to describe the behaviour of the swirling gas flow through and downstream the EIGA gas nozzle and to highlight the influence of the main operating parameters on the jet characteristics. The developed model is based on the Reynolds-Averaged Navier-Stokes (RANS) approach using the Favre decomposition for compressible flow together with a k-ω SST turbulence model. The numerical results are partially validated against images of the gas flow patterns obtained using the Schlieren imaging technique. The simulation results show that the gas flow transits to a supersonic regime immediately before exiting the nozzle. In the atomization tower, it forms a swirling supersonic jet with an asymmetric geometry composed of several Mach diamonds. The inlet gas pressure has a significant effect on the jet structure and Mach number distribution. However, within the investigated range of pressure values (30 to 45 bar), the swirling motion of the jet, hence the jet geometry, remain little affected. In contrast, a small increase of the nozzle exit slit size significantly increases the swirling motion, which in turn strengthens the jet asymmetry. A reduction of the overpressure in the melting chamber has a similar effect, but to a lesser extent.

Key words: Free-fall atomizer, swirling supersonic gas flow; metal powder; numerical simulation; Mach diamond, Schlieren technique

1. Introduction

The rapid growth in recent years of additive manufacturing techniques for metal parts, particularly in the aerospace and automotive industries, has stimulated a strong demand for metal powders, especially fine particles of high sphericity. A widely applied and cost-effective method to produce such metal powders is gas atomization (Yule, et al., 1994). In this process, a stream of liquid metal, which may be produced by different melting techniques (induction, plasma, electric arc), comes into contact with one or more high pressure gas jets, resulting in the breakup of the metal stream into small droplets, which subsequently solidify to form powder

particles. Gas atomization processes can be classified, according to the nozzle configuration, into close-coupled type and free-fall type (Li, et al., 2017). The close-coupled type is characterized by a high proximity of the gas nozzle and the melt delivery nozzle, which allows achieving a higher yield of fine particles. Yet this configuration is prone to harmful phenomena, such as clogging of the melt nozzle or disruption of the flow of the molten stream. In contrast, the free-fall type, owing to a greater separation of the gas and melt nozzles, is less sensitive to these latter issues and easier to operate. However, it produces fewer fine particles.

In this paper, the system under study is a particular free-fall atomization process called Electrode Induction melting Gas Atomization (EIGA) (Hohmann, et al., 1991). This process combines the melting of a rod shape metal electrode using a crucible-free induction heating technique and free-fall atomization by means of a supersonic high-pressure inert gas jet. Non-contact induction melting limits any process-related metal pollution, allowing the production of ultra-clean powders, which makes the EIGA process particularly well suited for the manufacturing of powders of easily oxidized and highly reactive metals (such as titanium alloys) (Sun, et al., 2017) (Wei, et al., 2017). Some EIGA units (such as the one considered in the present study) are equipped with a swirling gas nozzle, yet the impact of the swirl motion of the gas on the characteristics of the produced particles is not clearly understood. The particle size distribution of powders prepared by EIGA ranges typically from 1 to about 300 µm (Deborde, et al., 2019) (Drawin, et al., 2020).

Until now, gas atomization processes with close-coupled configuration has drawn the majority of research interest, with an increasing number of studies making use, in recent years, of CFD modeling techniques. A first group of studies focused on gas flow patterns without considering the liquid metal phase. Most of these studies aimed at evaluating the influence of various designs of the melt and gas nozzles. They relied on solving the compressible Navier-Stokes equations and the energy transport equation, coupled with a turbulence model. Motaman et al. (Motaman, et al., 2015) reported a single-phase gas flow model, which was verified against gas flow images obtained by means of the Schlieren technique. More recently, Urionabarrenetxea et al. (Urionabarrenetxea, et al., 2021) examined numerically the effects on the gas flow dynamics of various nozzle design related parameters, including the addition of swirling to the atomizing gas. They found that the gas swirling motion causes the supersonic gas plume to be shorter and wider, which might be detrimental for producing fine powder particles.

A second major group of studies focused on the complex interactions between the gas and the liquid metal stream, considering fragmentation and atomization phenomena of the metal. Zeoli et al. (Zeoli , et al., 2011) concentrated on metal atomization in the immediate vicinity of the nozzle exit, comparing the performance of three different nozzle geometries. An Eulerian approach based on the VOF (Volume Of Fluid) technique was used to track the evolution of the gas-metal interface. Their results suggested that a swirling gas nozzle stabilizes the melt core, which influences negatively the atomization process. The effect of shock-waves produced in the gas flow on the secondary fragmentation of pre-generated droplets was studied by (Kaiser, et al., 2018). The droplets were treated as discrete particles (Lagrangian framework) considering a two-way coupling with the gas flow model. This study concluded that shock waves have a negative impact on the production of fine particles. In (Odenthal, et al., 2021), the flows of gas and metal close to the nozzle exit were modelled using a simplified Euler-Euler approach, while secondary breakup in the far field was computed with a Lagrangian approach, considering only one way coupling with the gas flow. As part of this study, computed flow patterns for pure gas flow and for two-phase flow, in the case of a water-air system, were compared with experimental focusing Schlieren images (Vogl, et al., 2019). A simulation covering the whole atomization process was also reported by (Li, et al., 2017), combining a VOF approach for the primary breakup near the melt nozzle and a Lagrangian approach for the subsequent particle fragmentation. However, these coupled approaches

prove to be complex to implement and costly in terms of computation time, while not allowing to represent the whole phenomena.

Only a limited number of studies that deal with free-fall nozzles have been reported in the literature. Moreover, most of these studies consider a non-swirling gas jet. The numerical investigation of (Fritsching, 2005) focused on the dynamics of the gas flow as a function of the nozzle shape. In (Hulme-Smith, et al., 2021), 2D numerical simulation results of a pure gas flow from a De Laval nozzle under typical atomization conditions were compared with experimental data obtained using shadowgraphy. Yet, some discrepancies between the predicted and observed number of Mach diamonds in the gas jet were identified. Considering a simplified 2D axisymmetric geometry, (Zou, et al., 2021) investigated numerically the complete fragmentation process of a single drop, combining an Eulerian VOF model and an Eulerian-Lagrangian model.

As a first step towards a complete modeling of the EIGA process, the present work describes a numerical model to simulate the gas flow dynamics through the gas nozzle and inside the atomization chamber, which plays a crucial role in understanding the atomization process. The objective of this work is to investigate the effects of various gas related operating parameters (gas supply pressure and nozzle geometry), as well as to better understand the influence of the gas swirl motion, which is a point that has little been addressed in the literature. The numerical work is complemented by visualization experiments of the gas flow patterns using the Schlieren imaging technique, which are used to verify the predictions of the numerical model. This numerical model will be a support for the industry to better characterize the gas flow patterns and optimize the efficiency of the gas nozzle, with the final aim to improve the performance of the atomization process, such as increasing the yield of fine powders.

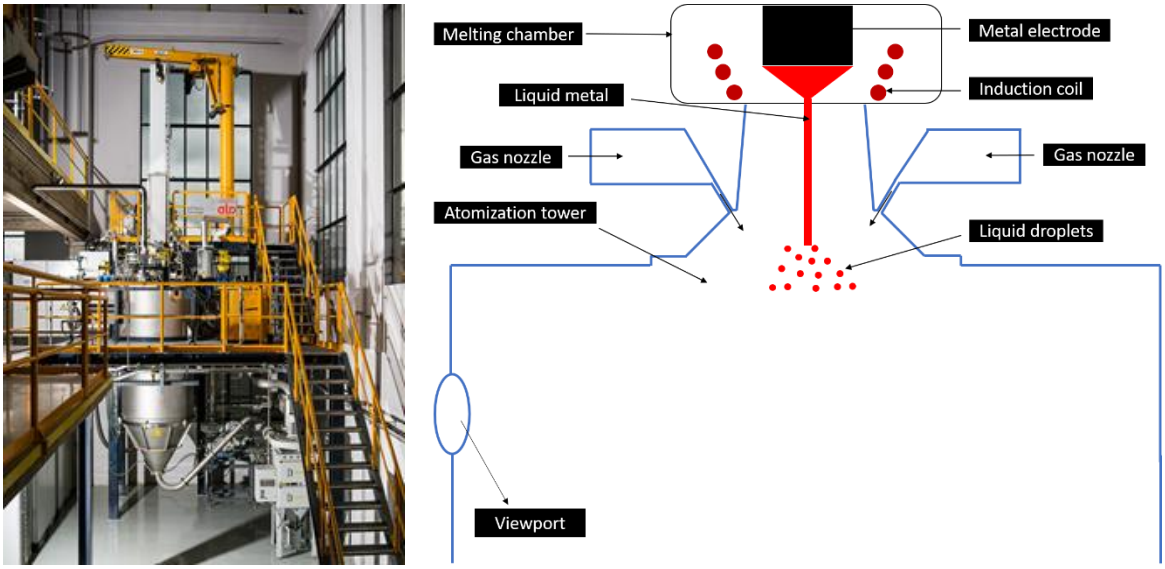

Figure 1 : Left: View of the EIGA atomization tower installed at MetaFensch. Right: schematic of the EIGA atomization process showing the melting and free fall of metal and its atomization into droplets.

2. Experimental setup

2.1. EIGA atomization tower

The experiments and simulations reported in the present study refer to the EIGA facility (ALD Vacuum Technologies GmbH, Hanau, Germany) installed at MetaFensch (Uckange, France), which is shown schematically in Figure 1. It includes three main sections, namely the gas nozzle, the melting chamber and the atomization tower. The gas nozzle is responsible for generating a high-speed gas jet. It is composed of two tangential gas inlets of diameter 12 mm, that enable to impart a swirl motion to the gas flow. The gas exits the nozzle through a convergent annular slit with a width of 0.7 mm. In the melting chamber, a rod-shaped metal electrode is melted, without contact, into a conical induction coil. The produced molten metal flows vertically through a free-fall melt delivery nozzle and is impacted by the swirling high velocity gas jet in the atomization tower. The metal is disintegrated into liquid droplets, yielding after solidification to metal powder particles. In order to control the free-falling molten metal flow and prevent issues such as clogging phenomena and metal droplet backflow, the gas pressure in the melting chamber is maintained slightly higher than that in the atomization tower. The molten metal flow can be either a continuous stream or a discontinuous flow of drops (Zou, et al., 2021) depending on the rotation and feeding speed of the electrode and the electrical power in the induction coil. Since the present EIGA facility is applied to the production of reactive alloys (such as Ti alloys), the inert gas argon is used as atomization gas. The present facility enables to atomize electrodes with a maximum length of 1000 mm and with three different diameters of 70, 100 and 150 mm, which corresponds to the production of about 15, 30 and 75 kg of Ti powders respectively.

2.2. Schlieren technique in the EIGA tower

The Schlieren imaging technique is applied in the MetaFensch EIGA facility to visualize the high velocity gas flow downstream the gas nozzle. The measurements are performed on a pure gas flow and are used to verify the results of our CFD model. The Schlieren technique, is a standard tool to investigate compressible flows (Motaman, et al., 2015) (Luh, et al., 2018). It relies on the Gladstone-Dale equation, which relates the local refractive index to the local gas density. Any gas density gradients result in a change in the refractive index of the gas, which is converted into variations of light intensity by means of the Schlieren setup. Detailed information about the principle and implementation of the Schlieren technique can be found in (Settles, 2001).

Because the EIGA facility does not include two diametrically opposite viewing ports and due to the fact that the viewing ports are located at 420 mm downstream the nozzle outlet, the Schlieren setup employed in the present study differs slightly from conventional setups described in the literature. The schematic of the actual setup employed is shown in Figure 2. The setup consists of a LED point source light and a HD camera positioned in front of a viewing port. Inside the tower, two plane mirrors acting as a periscope to observe the gas flow as close as possible to the exit of the nozzle and one parabolic mirror of a focal length equal to 1 m are installed. The camera used in this study is a full frame hybrid digital camera Nikon Z6. The ISO setting is fixed at 30000, the camera opening is set to 2.8 and the exposure time is chosen to be 0.125 ms. The optical distance from the parabolic mirror to the camera is set to twice the focal length of the mirror. Additionally, a horizontal razor blade is placed in front of the camera, which served as a cut-off of the undeflected light, in order to improve contrast and visualize gas density axial gradients. The gas flow region observed using the present arrangement is situated from an axial distance of 29 mm downstream of the nozzle exit.

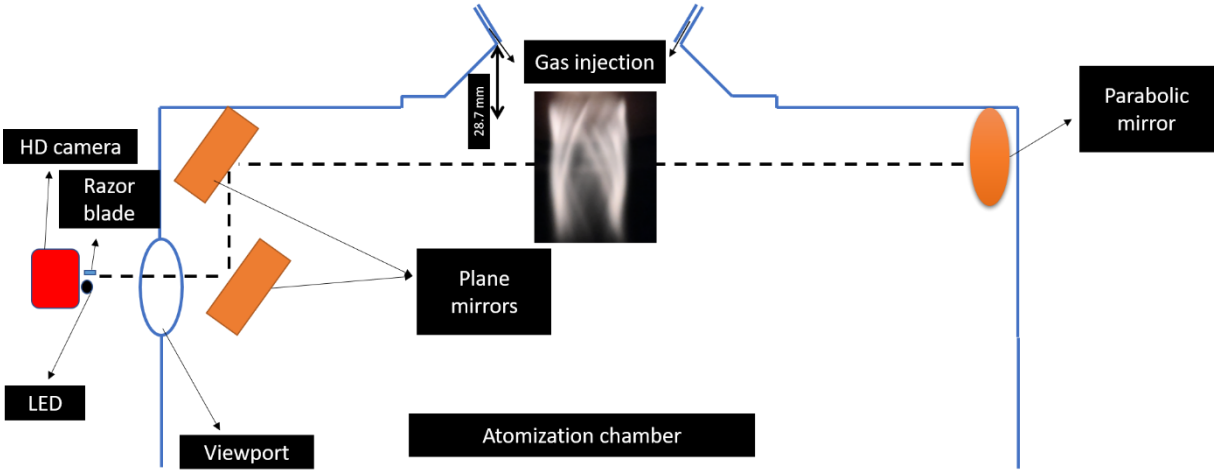

Figure 2 : Schematic of the Schlieren experimental setup used to visualize the gas flow field inside the EIGA tower.

3. Flow modeling

A numerical model is developed within the Computational Fluid Dynamics software ANSYS-Fluent 2021R1 to describe the gas flow through and downstream the gas nozzle, with consideration of compressibility, swirling and turbulence effects. In this section, we first present the governing equations, followed by the boundary conditions and the numerical methods.

3.1. Governing equations for compressible flow

The gas flow considered in this study is compressible, turbulent, three dimensional and stationary. To keep the computational cost reasonable, the governing equations for mass, momentum and energy conservation are solved using the Reynolds-Averaged Navier-Stokes (RANS) approach, which introduces a decomposition of flow quantities into time averaged values and time varying fluctuations and considers time average conservation equations. In compressible flow studies, all flow variables are decomposed using the Favre averaging approach, except density and pressure, which are decomposed through the Reynolds approach ($f = \bar{f} + f'$, where $\bar{f}$ is the mean value and f' is the turbulent fluctuation) (Hinze, 1975). The Favre decomposition is defined as $f = \hat{f} + f''$, where $\hat{f}$ is the mass weighted average ($\bar{\rho}\hat{f} = \overline{\rho f}$) and f'' is the turbulent fluctuation according to Favre approach. The averaged governing equations can be written as follows (Huang, et al., 1995):

$$\frac{\partial(\bar{\rho}\widehat{u_i})}{\partial x_i} = 0 \qquad (1)$$

$$\frac{\partial(\bar{\rho}\widehat{u_j}\widehat{u_i})}{\partial x_j} = -\frac{\partial \bar{P}}{\partial x_j} + \frac{\partial}{\partial x_j}\left(\widehat{\tau_{ij}} + \widehat{\tau_{ij}^R}\right) \qquad (2)$$

$$\frac{\partial(\bar{\rho}\widehat{u_j}\widehat{H})}{\partial x_j} = \frac{\partial}{\partial x_j}\left[\widehat{u_i}\left(\widehat{\tau_{ij}} + \widehat{\tau_{ij}^R}\right)\right] + \frac{\partial}{\partial x_j}\left[\lambda\frac{\partial \widehat{T}}{\partial x_j} - \bar{\rho}\widehat{u_j''h''} + \widehat{\tau_{ij}u_i''} - \bar{\rho}\frac{\widehat{u_j''u_i''u_i''}}{2}\right] \qquad (3)$$

Where $\bar{\rho}$, $\hat{u}$, $\bar{P}$ and $\hat{T}$ are the mean density, velocity, pressure and temperature respectively. The subscripts i, j, k refer to the space directions. $\widehat{\tau_{ij}} = \mu[\frac{\partial(\widehat{u_i})}{\partial x_j} + \frac{\partial(\widehat{u_j})}{\partial x_i} - \frac{2}{3}\frac{\partial(\widehat{u_k})}{\partial x_k}\delta_{ij}]$ is the stress tensor and $\widehat{\tau_{ij}^R} = -\bar{\rho}\widehat{u_i''u_j''}$ is the Reynolds stress tensor. μ and λ are the dynamic viscosity and

the thermal conductivity respectively. $\widehat{\boldsymbol{H}} = \hat{\boldsymbol{e}} + \frac{\bar{\boldsymbol{P}}}{\bar{\boldsymbol{\rho}}} + \boldsymbol{k}$ is the mean total enthalpy and $\boldsymbol{k} = \frac{\boldsymbol{1}}{\boldsymbol{2}} \widetilde{\boldsymbol{u_i''} \boldsymbol{u_i''}}$ is the turbulent kinetic energy. $\hat{\boldsymbol{e}}$ is the mean internal energy and $\widehat{\boldsymbol{h}}$ is the specific enthalpy.

The k-ω shear-stress transport (SST) turbulence model (Menter, 1994) is used to close the Reynolds stress tensor term in the above equations. This model behaves as the k-ω turbulence model in near-wall regions and as the k-ε turbulence model in far-field regions, ensuring an accurate calculation of the turbulence everywhere in the computational domain. This model of turbulence was used in several other studies dealing with flow fields similar to the one considered in the present work (Vogl, et al., 2019) (Ridolfi, et al., 2020). Since our model deals with high speed flows, the Wilcox's compressibility correction in the dilatation-dissipation term in the k-ω SST equations (Rumsey, 2010) is considered in this study.

3.2. Boundary conditions and numerical methods

The 3D computational domain inside which gas flow is simulated is based on the MetaFensch EIGA facility described in section 2.1 and is illustrated in Figure 3. It consists of a gas nozzle connected to a cylinder of diameter 150 mm and height 200 mm representing a portion of the atomization tower. The real geometry of the gas nozzle was modelled in SolidWorks and transferred to Ansys-Fluent software.

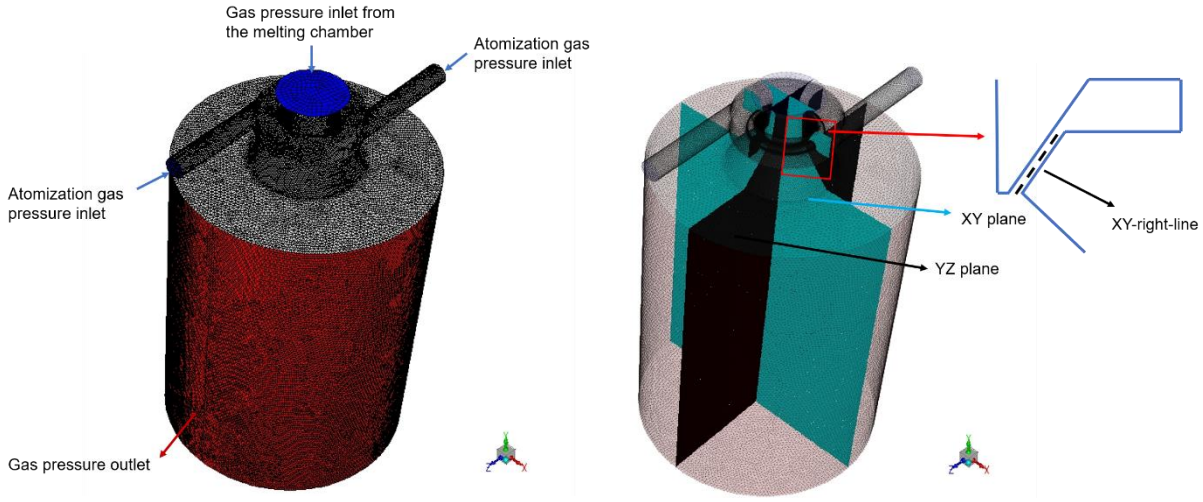

Figure 3 : Left: view of the meshed computational domain and its boundary conditions. Right: visualization of the position of the XY and YZ planes and of the centerline in the nozzle annular slit (referred as XY-right-line).

As far as boundary conditions are concerned, a pressure inlet condition is considered on the two nozzle inlets and on the top surface connecting the melt chamber and the atomization tower. All cylinder surfaces are handled as gas outlets (pressure outlet condition), except the top annular surfaces of the cylinder which are treated as a wall. On the gas inlets, the turbulent

intensity is imposed and estimated from the Reynolds number using the following expression: $I = 0.16Re^{-0.125}$ (Hulme-Smith, et al., 2021).

Figure 3 (right) highlights the XY and YZ planes, respectively perpendicular and parallel to the nozzle inlets, where the numerical results will be reported. Some numerical results will be also presented along the centreline of the annular slit at the nozzle outlet, as shown in the zoom in Figure 3 (right).

The simulations reported in this study are performed using a density-based solver with an implicit formulation. The second-order upwind scheme is applied for spatial discretization of the equations, while the Advection Upstream Splitting Method (AUSM) is used to calculate the convection fluxes. The Courant number is set to 1 to ensure the computation stability.

4. Results and discussion

The argon atomizing gas is treated as an ideal gas. Its thermophysical property are provided in Table 1. In this section, we present the numerical results corresponding to six simulation cases, whose input parameters are listed in Table 2. The gas pressure at the nozzle inlet is changed between 30 and 45 bar, the gas pressure in the melting chamber is varied between 1 and 1.6 bar, while the gas temperature in all simulations is fixed to 274 K at the nozzle inlet and to 300 K at the top and outlet boundaries (in case of gas backflow). The slit size at the nozzle outlet is varied between 0.6 and 0.8 mm.

To capture precisely the features of the high-velocity gas flow, a fine mesh is required. The computational mesh employed in this study is composed of 5.17 to 5.34 million tetrahedral cells, including 1.2 million cells in the nozzle portion. Mesh convergence has been checked.

We first present results concerning test case #1 and discuss in detail the gas flow behaviour in the entire system including the gas nozzle and the atomization tower. A comparison between the model predictions for test case #1 and the image obtained using the Schlieren experimental technique is also discussed. Then, the model is employed to investigate the influence of the inlet gas pressure, the nozzle exit slit size, and the gas pressure in the melting chamber on the gas flow patterns, with a particular focus on the swirling motion of the gas.

Table 1 : Argon thermophysical properties used in this study

Thermophysical properties	Molecular Weight (kg. kmol^{-1})	Specific heat (J.kg^{-1}. K^{-1})	Thermal conductivity (W.m^{-1}. K^{-1})	Dynamic viscosity (Pa.s)
Argon	39.95	520.64	0.0158	2.125 * 10^{-5}

Table 2 : Operating parameters of the six simulation test cases.

Simulation run	Nozzle inlet gas pressure (bar)	Nozzle inlet gas temperature (K)	Gas pressure in the melting chamber (bar)	Gas temperature in the melting chamber (K)	Outlet gas pressure (bar)	Nozzle exit slit size (mm)
#1	45	274	1.2	300	1	0.7
#2	30	274	1.2	300	1	0.6
#3	30	274	1.2	300	1	0.7
#4	30	274	1.2	300	1	0.8
#5	30	274	1	300	1	0.7

#6	30	274	1.6	300	1	0.7

4.1. Simulation of a validation case (Case #1)

The simulation reported in this subsection corresponds to test case #1 in Table 2: The gas pressure at the nozzle inlet is 45 bar, the gas pressure in the melting chamber is 1.2 bar, and the slit size is 0.7 mm.

4.1.1. Gas flow in the nozzle

The gas velocity vectors throughout the nozzle, coloured by the Mach number of the gas flow field and by the gas density, are shown in Figure 4 (left) and (right), respectively. The gas flows with relatively homogeneous Mach number and density values through the majority of the nozzle, with the gas flow regime remaining subsonic. The flow regime alters suddenly close to the nozzle exit as a result of the convergent shape of the nozzle exit slit. The density of the gas drops abruptly and the Mach number increases sharply, resulting in a transition from a subsonic to a supersonic flow regime.

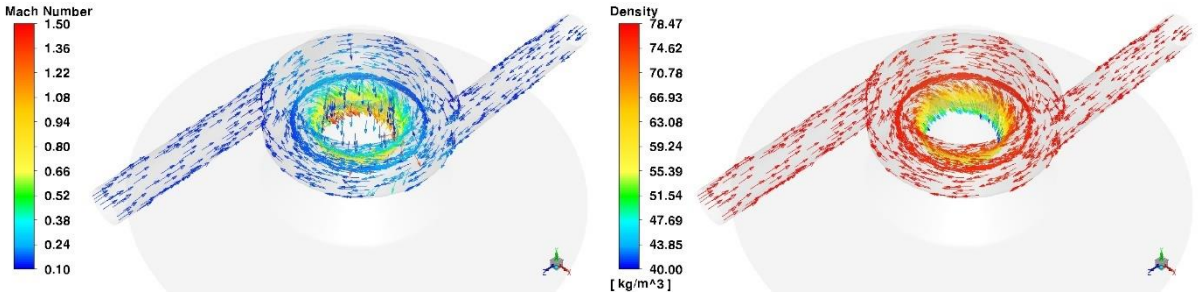

Figure 4 : Gas velocity vectors in the nozzle coloured by (left) the Mach number and (right) the gas density.

In order to locate precisely the position of the sonic transition, the evolution of the Mach number along the centreline of the exit slit is plotted in figure 5 (left). Results are presented in four different vertical planes 90° apart. The Mach number ranges from 0.55 at the slit entrance up to 1.25 at the nozzle exit. The sonic transition occurs 0.55 mm before the exit. Where the gas flow is subsonic, the Mach number in the inlet perpendicular plane (XY plane) is higher than the one in the inlet parallel plane (YZ plane), while Mach number values are similar in both planes downstream the sonic transition.

To quantify the strength of the gas swirl motion, a non-dimensional swirl number, defined as the ratio of the azimuthal velocity to the axial velocity (u_z/u_{ax}) (Oberleithner, et al., 2007), is introduced. Figure 5 (right) presents the evolution of this number along the exit slit centreline in the same four planes considered in figure 5 (left). The swirl number decreases along the exit slit, with values varying between 0.72 and 0.33, which corresponds to a fairly weak swirling flow (Loiseleux, et al., 2003). The swirl number in the XY plane (perpendicular to the inflow) is

approximately 15% larger than that in the YZ plane (parallel to the inflow). This difference is a direct consequence of the non-axisymmetry of the tangential gas feeding system.

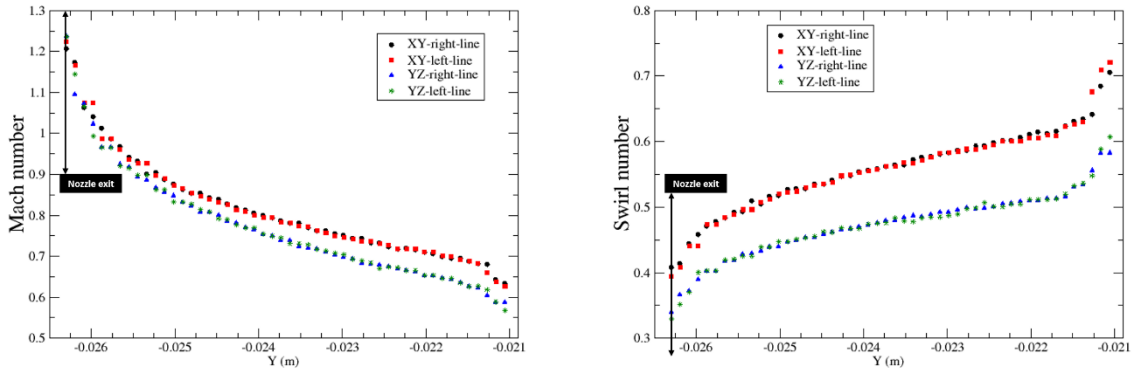

Figure 5 : Evolution of the Mach number and swirl number along the centreline of the exit slit of the nozzle in four different vertical planes 90° apart. The gas flows from the coordinate Y= -0.021 m to the coordinate Y=-0.0263 m.

To characterize the evolution of the gas state between the nozzle inlets and outlet, the values of the principal gas variables averaged across each of these surfaces have been calculated and are reported in Table 3. As a result of the head losses in the nozzle, the total pressure falls by about 4% at the nozzle outlet. Similarly, the static pressure, static temperature and the density are reduced by 67 %, 34 % and 49 %, respectively, while the velocity magnitude and the Mach number are multiplied by a factor of 8 and 9 compared to their inlet values. The gas volume flow rate predicted by our model is 1638 Nm^3/h. This latter value is consistent but does not match exactly the volume flow rate measured in the MetaFensch EIGA unit under these particular conditions (namely 1300 Nm^3/h). The 20% discrepancy between the simulation and experimental results is likely related to the pressure losses in the gas supply pipelines between the nozzle inlet and the precise location of the flowmeter and pressure sensor (significantly upstream the nozzle inlets). As a consequence, the actual gas pressure at the nozzle inlet is probably slightly lower than the value of 45 bar used in our simulation.

Table 3 : Values of the gas variables averaged across the inlet and outlet surface of the nozzle and comparison of numerical values of static pressure and temperature at the nozzle outlet with values determined from the isentropic flow theory.

Nozzle	Total pressure (bar)	Static pressure (bar)	Static temperature (K)	Density (kg/m^3)	Velocity Magnitude (m/s)	Mach number	Swirl number	Volume flow rate (Nm^3/h)
Inlet	45	44.3	272.3	78.2	41.6	0.14	-	1638
Outlet	43.1	14.9	178.8	39.8	314.8	1.27	0.35	1638
Isentropic relations	-	15.4	178.7	-	-	-	-	-

The slight decrease of the total pressure in the nozzle implies that the flow is not strictly isentropic. In order to quantify the deviation from isentropic state, we compare in Table 3 the values of the static pressure and temperature at the nozzle outlet predicted by our model with that computed using the relations below for isentropic flow (i.e. considering that the total pressure and the total temperature remain constant):

$$\frac{T_{out}}{T_{in}} = \frac{1 + \frac{\gamma - 1}{2} M_{in}^2}{1 + \frac{\gamma - 1}{2} M_{out}^2} \quad (4)$$

$$\frac{P_{out}}{P_{in}} = \frac{\left(1 + \frac{\gamma - 1}{2} M_{in}^2\right)^{\frac{\gamma}{\gamma - 1}}}{\left(1 + \frac{\gamma - 1}{2} M_{out}^2\right)^{\frac{\gamma}{\gamma - 1}}} \quad (5)$$

where γ is the specific heat ratio (γ=1.667 for argon). Our results match those obtained using the isentropic equations with a very small difference, namely 0.1% and 3.8% for temperature and pressure respectively. Therefore, deviation from isentropy remains small and a good approximation of the static pressure and temperature at the nozzle outlet may be obtained from the relations (4) and (5).

4.1.2. Gas flow in the atomization tower

As shown in the previous section, the gas exits the nozzle towards the atomization tower with a swirl motion. Figure 6 shows the gas jet envelope in the atomization tower coloured by the swirl number in two different views. The flow envelope corresponds to the isocontour of ambient argon density (i.e. 1.76 kg/m3). Due to the non-axisymmetry of the gas feeding system, a highly asymmetric jet geometry is formed. Because the swirl number at the nozzle exit is higher in the plane perpendicular to the gas inlets, the jet is wider in the X direction. It is also observed that the widening of the jet in the X direction intensifies from a distance of about 130 mm from the nozzle top. Moreover, the swirl number decreases in the Y vertical direction. In Figure 6 (right), it can be seen that the jet has an annular type shape, with an inner core region including separate low-density gas regions. This core formation is related to the action of the series of compression-expansion waves occurring downstream the nozzle as described below.

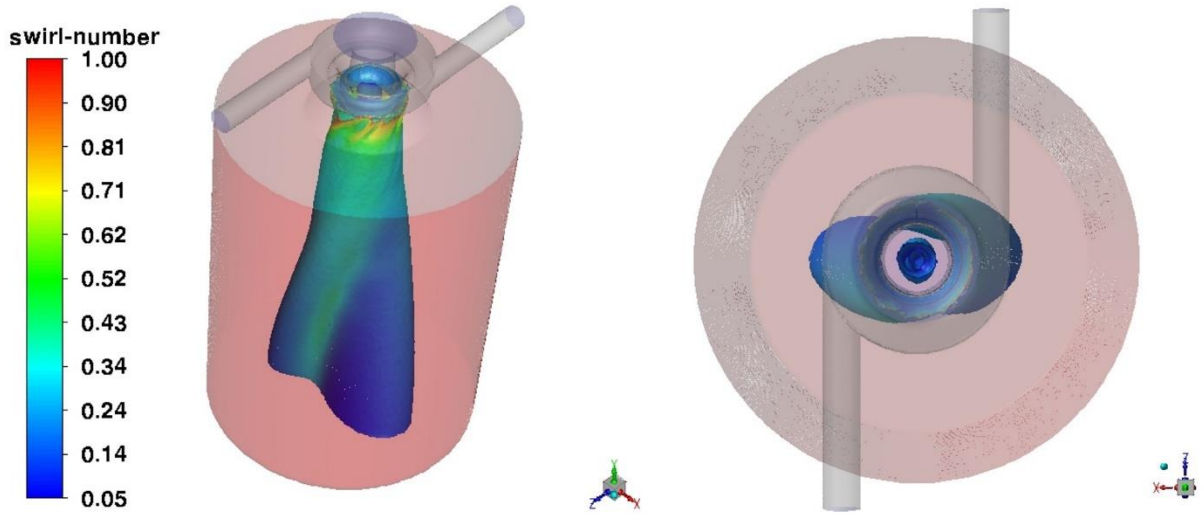

Figure 6 : Visualization of the gas jet envelope in the atomization tower coloured by the local swirl number: XYZ view (left) and XZ view (right). The envelope is defined from the ambient Ar density isocontour.

The gas flow leaves the nozzle in a supersonic regime. The mismatch between the pressure of the gas jet at the nozzle exit and the ambient pressure in the atomization tower induces the repetition of expansion-compression wave patterns. This leads to the formation of classic small cellular structures similar to Mach diamonds through which the gas undergoes a series of acceleration and deceleration. Those structures are clearly visible in Figure 7 and Figure 8 (left), which show respectively the distributions in the atomization tower of the flow Mach number and the static pressure. Each “Mach diamond” is enclosed by inner and outer shear layers. The highest value reached by the Mach number is about 5 and is located immediately downstream the nozzle exit within the first Mach diamond. The dimensions of the first Mach diamond are significantly smaller than those of the second and third Mach diamonds. Figure 8 (right) shows the profiles of the Mach number and the static pressure along the symmetry axis. One observes that a horizontal shock develops at the level of the second Mach diamond (Y = -0.075 m). This shock, known as a Mach disk (Vogl, et al., 2019), is also clearly visible in Figure 7.

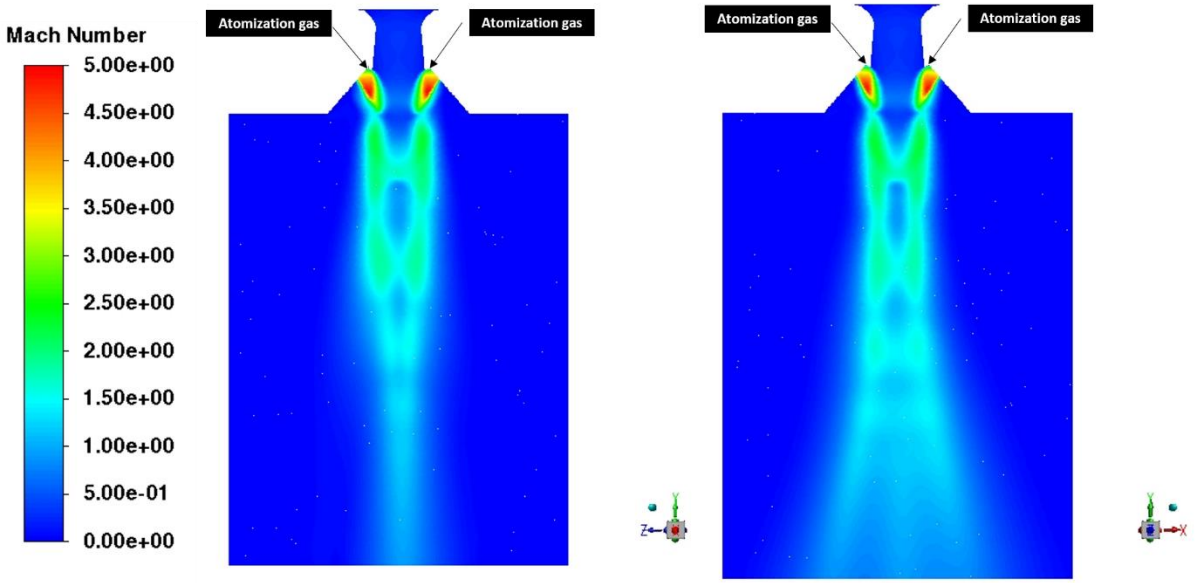

Figure 7 : Distribution of the flow Mach number in the YZ (left) and XY (right) planes.

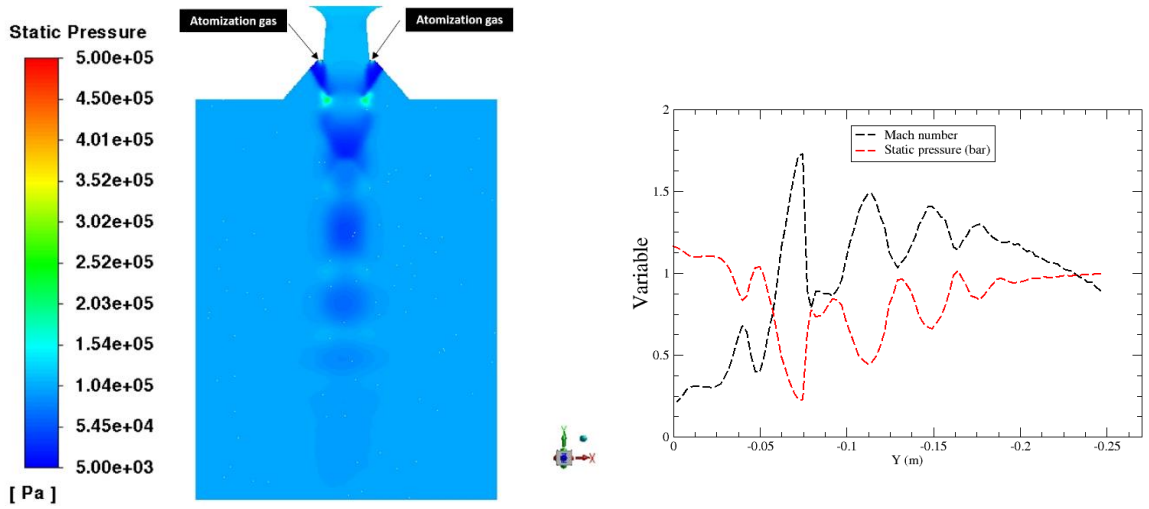

Figure 8 : Left: distribution of static pressure in XY plane. Right: profiles of the Mach number and static pressure along the symmetry axis. The gas flows from Y= 0 m (top nozzle) to Y=-0.25 m.

Downstream the third Mach diamond, the behaviour of the gas jet deviates significantly in the XY and YZ planes, resulting, as already observed in Figure 6, in the reinforcement of the jet asymmetry. This phenomenon is related to the decrease of the swirl number in the X direction whereas it remains significant in the center of the YZ plane. The kinetic energy of the gas significantly reduces along the flow directions from the fourth Mach diamond. It can be seen in Figure 8 (right) that a cycle of four compression-expansion waves evolves between each Mach diamond. The Mach number decreases definitively below the sonic point at a distance of 225 mm from the top nozzle, resulting in a pure subsonic gas flow.

As observed in the above figures, the swirling motion is responsible for a strong asymmetry of the gas jet. Such an asymmetry of the gas jet is associated to a reduction of the horizontal distance between the Mach diamonds, which increases the overall gas kinetic energy in the core of the gas jet. This should be favorable for the metal atomization, as the molten jet will interact with a higher kinetic energy gas.

Finally, the results of our simulation are compared to the image of the gas flow field in the MetaFensch EIGA unit obtained using the Schlieren visualization technique. As discussed in Section 2, the position of the viewports in the EIGA facility enables to visualize a region starting only from a distance of 0.055 m from the top boundary, which prevents us to observe the first Mach diamond. The recorded Schlieren image contains information on the density axial gradients arising throughout the whole optical path of the studied domain. For simplicity, as an initial consideration, we present in Figure 9 only a comparison of the Schlieren image with the calculated density axial gradients in the mid-plane of the geometry, without depth averaging. The ambient density isocontour of 1.76 kg/m3 is superimposed on the figure to identify the external boundary of the gas jet. A good consistency between the Schlieren image and the simulation results is achieved. In particular, the radial dimension of the jet, the vertical dimension of the second Mach diamond and the position of the Mach disk associated to the second diamond are correctly predicted by the numerical simulation. The Mach disk is located approximately 43 mm downstream of the nozzle exit and the second vertical Mach diamond ends about 63 mm downstream of the nozzle exit in both the numerical and experimental studies.

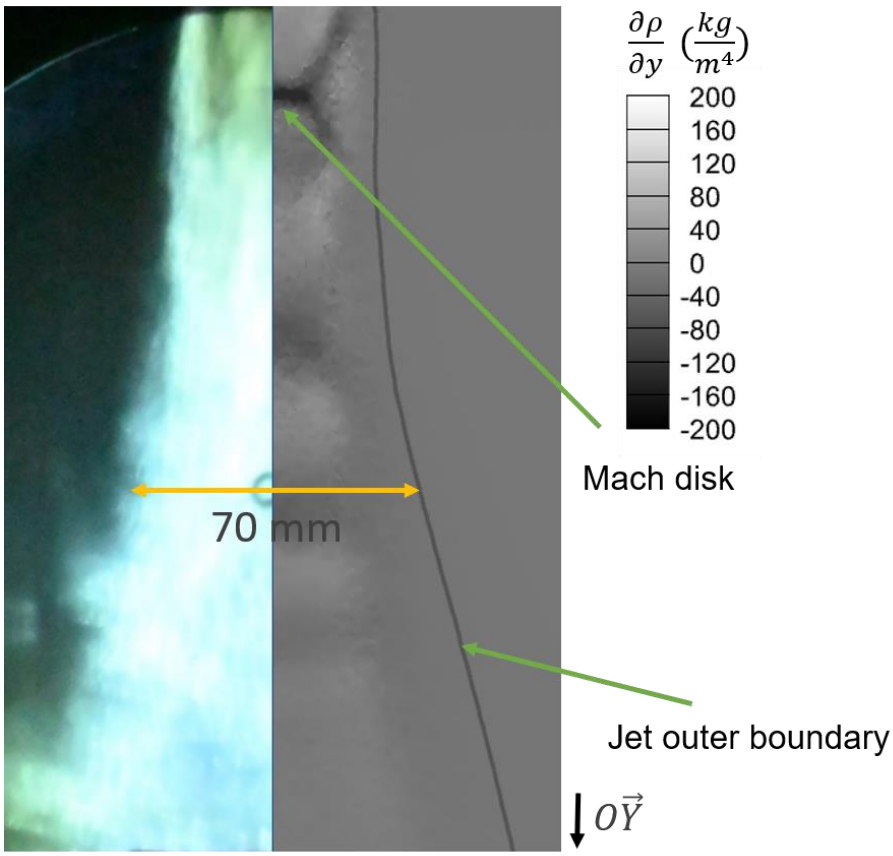

Figure 9 : Comparison of experimental Schlieren image (left) and computed gas density vertical gradients (right).

4.2. Effect of nozzle exit slit size

In this section, the influence of the nozzle exit slit size on the gas flow is highlighted from the simulation results of test cases #2, #3 and #4 in Table 2. The gas pressure at the nozzle inlets is 30 bar, the gas pressure in the melting chamber is 1.2 bar and the slit size ranges from 0.6 to 0.8 mm.

Figure 10 reports the profiles of Mach number (left) and swirl number (right) along the centreline of the nozzle exit slit in the right half of the XY plane (XY-right-line) for simulations #2, #3 and #4. Except close to the nozzle exit, the Mach number slightly grows as the slit size increases. Its value for a slit of 0.8 mm is about 7% higher than that for a slit of 0.6 mm. As a consequence, the sonic transition occurs earlier with the increase of the slit size. Similarly, the swirl number increases as the slit size increases, yet the effect is more important than that on the Mach number. The swirl number for a slit of 0.8 mm is approximately 25% higher than that for a slit of 0.6 mm.

Table 4 provides averaged values of the gas flow main variables at the nozzle inlet and outlet for the different slit sizes considered in this study. Increasing the slit size has a small influence on the head losses (i.e. pressure drop) in the nozzle. With the increase of the slit size, it can also be observed a slight decrease (resp. increase) of the temperature (resp. velocity magnitude) at the nozzle outlet, which leads to a slight increase of the outlet Mach number (about 1% when the slit grows from 0.6 to 0.8 mm). On the other hand, the slit size has a significant influence on the swirl number, increasing its value by about 25% when the slit grows

from 0.6 to 0.8 mm. This effect is mostly related to an increase of the velocity azimuthal component. Finally, the influence of the slit size on the volume flow rate is significant, with an increase of 30% when the slit size changes from 0.6 to 0.8 mm.

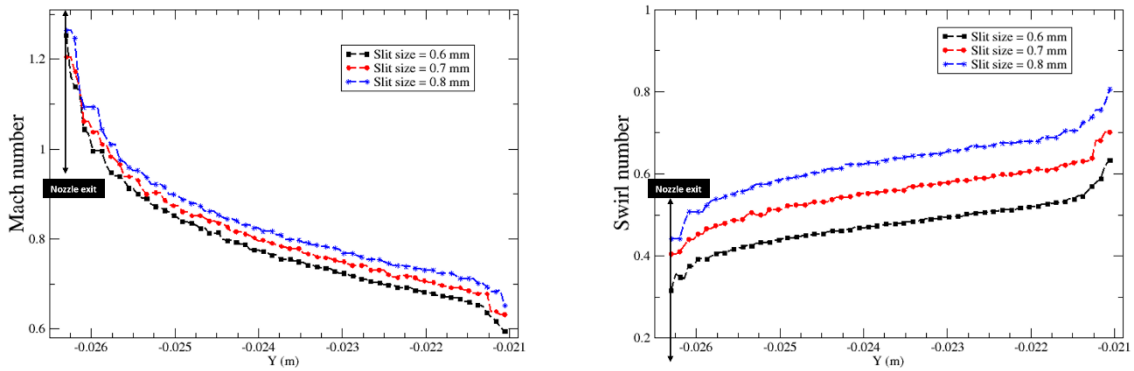

Figure 10 : Evolution of the Mach number and swirl number along the centreline of the exit slit of the nozzle in the right half of the XY plane (XY-right-line) for three different slit sizes. The gas flows from the coordinate Y= -0.021 m to the coordinate Y=-0.0263 m.

Table 4 : Averaged values of the gas flow main variables at the nozzle inlet and outlet computed for three different slit sizes.

Slit size (mm)	Nozzle surface	Total pressure (bar)	Static pressure (bar)	Static temperature (K)	Density (kg/m^3)	Velocity Magnitude (m/s)	Mach number	Swirl number	Volume flow rate (Nm^3/h)
0.6 (case #2)	Inlet	30	29.7	272.8	52.2	36	0.12	-	945
	Outlet	28.7	10	179.9	26.7	313.1	1.26	0.29	945
0.7 (case #3)	Inlet	30	29.5	272.3	52.1	41.5	0.14	-	1088
	Outlet	28.7	9.9	179	26.5	314.5	1.26	0.35	1088
0.8 (case #4)	Inlet	30	29.4	271.9	52	46.8	0.15	-	1224
	Outlet	28.6	9.7	177.8	26.2	316.4	1.28	0.39	1224

Figure 11 depicts the envelope of the gas jet, defined from the isocontour of the ambient argon density (i.e. 1.76 kg/m^3) and coloured by the swirl number for the three different slit sizes. As noted above, an increase in the slit size enhances the swirl motion, which leads to a more asymmetric jet geometry, namely the jet widens in the X direction and shrinks in the Z direction.

To quantify the more severe asymmetry of the gas jet when the slit size increases, the X and Z dimension ratio and the area of the cross-section of the jet at the bottom boundary of the

computational domain are reported in Table 5. When the slit size is increased from 0.6 to 0.8mm, it is observed that the X and Z dimension ratio is more than doubled while the jet cross-sectional area is increased by 30 %.

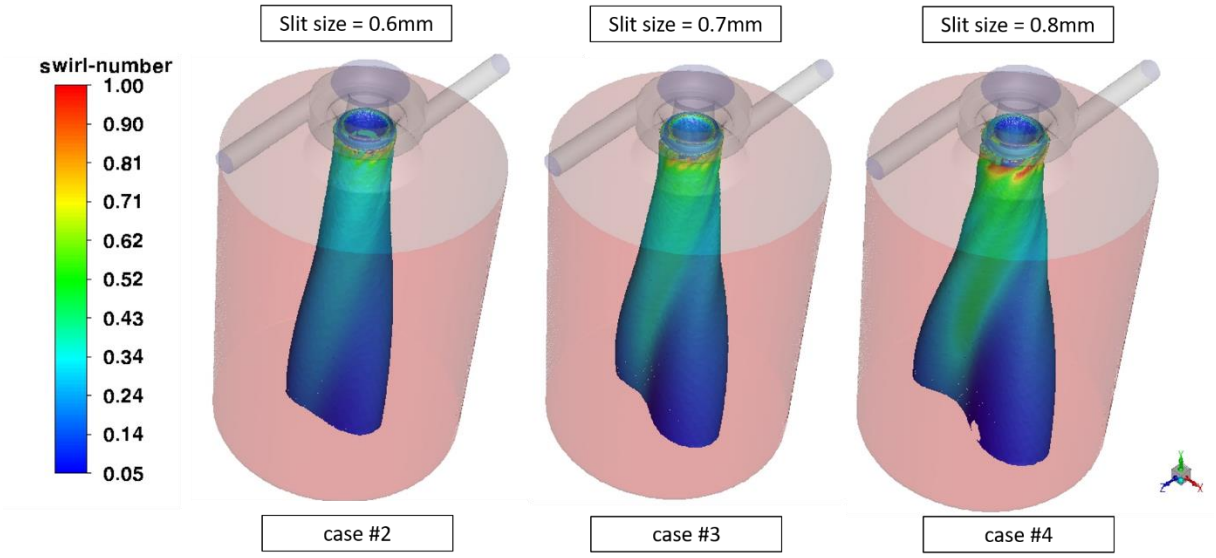

Figure 11 : Visualization of the gas jet envelope coloured by local swirl number for three different slit sizes. The envelope is defined from the ambient argon density isocontour.

Table 5 : Comparison of the X and Z dimension ratio and area of the cross-section of the jet at the bottom boundary of the computational domain computed for three different slit sizes.

Slit size (mm)	Surface (mm^2)	Lx/ Lz
0.6 (case #2)	1736	1.85
0.7 (case #3)	2120	2.87
0.8 (case #4)	2500	4.18

Figures 12 and 13 illustrate the distributions of the flow Mach number in the XY plane and along the symmetry axis of the atomization tower, for the three different slit sizes. Increasing the slit size causes an increase of the horizontal and vertical dimensions of the Mach diamonds, with greater maximum values of the Mach number reached in each diamond. It is also accompanied by an increase of the jet expansion in the X direction, which is a direct consequence of the stronger gas swirling motion for larger slit size, as noted in Table 4. Hence, the importance of the swirling motion and its impact on the gas flow in the atomization chamber intensify as the slit size is increased. While for slit sizes of 0.7 and 0.8 mm, the gas along the symmetry axis undergoes a series of compression and expansion waves, creating several separate supersonic regions, the gas flow for a slit size of 0.6 mm remains subsonic almost along the entire symmetry axis (where the liquid metal is supposed to fall) .

Results described above may be used to infer possible effects of the slit size on the gas/metal interactions and metal fragmentation in the EIGA process. Our numerical results indicate that larger Mach diamonds are generated when the slit size is increased. (Kaiser, et al., 2018)

found that a suitable metal flow path to produce fine droplets consists of the mother droplet flowing through the Mach diamond core. Therefore, one may conclude that increasing the slit size could be beneficial for the production of small size droplet. In addition, the greater Mach number values in the diamond observed for larger slit size would also favour the production of small size droplet. Indeed, on the basis of several experimental correlations (see for example the correlation derived by Rao and Mehrotra 1981 given below), it is well established that a higher gas velocity leads to a lower median particle diameter.

$$d_{50} = K\sqrt{\frac{\vartheta_m d_m \sigma}{\vartheta_g \rho_g U_g^2}\left(1+\frac{m_m}{m_g}\right)} \qquad (6)$$

K is a constant parameter specific to the system. The subscripts m and g correspond to the metal and the gas respectively. d_{50}, d, σ,ϑ and m correspond to the median particle size, the diameter of metal jet, the surface tension, the kinematic viscosity and the mass flow rate.

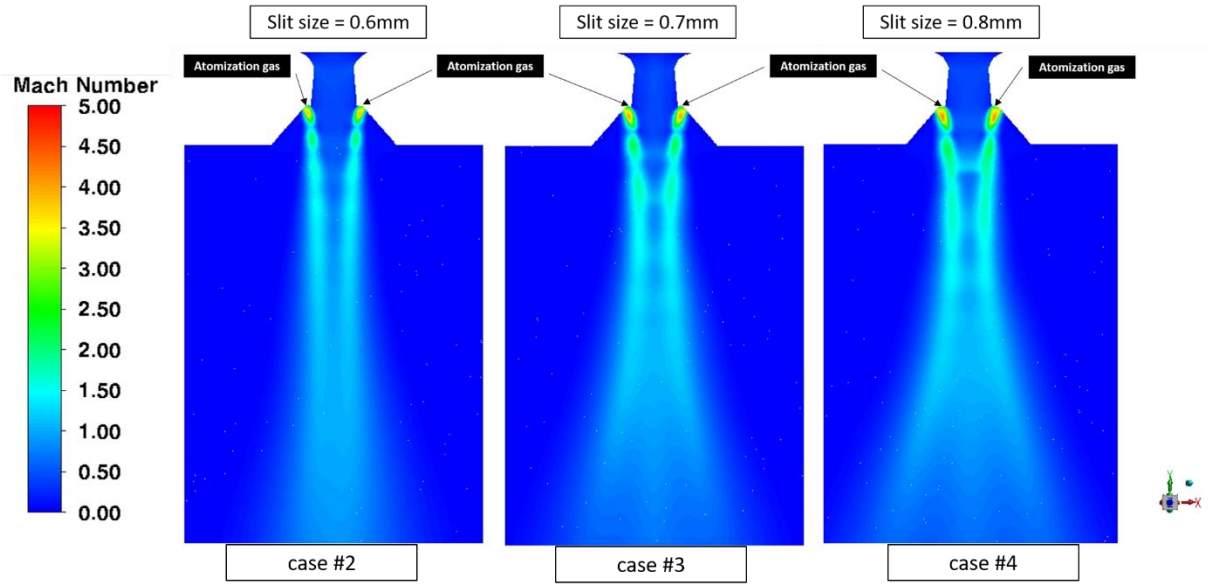

Figure 12 : Distribution of flow Mach number in the XY plane for three different slit sizes.

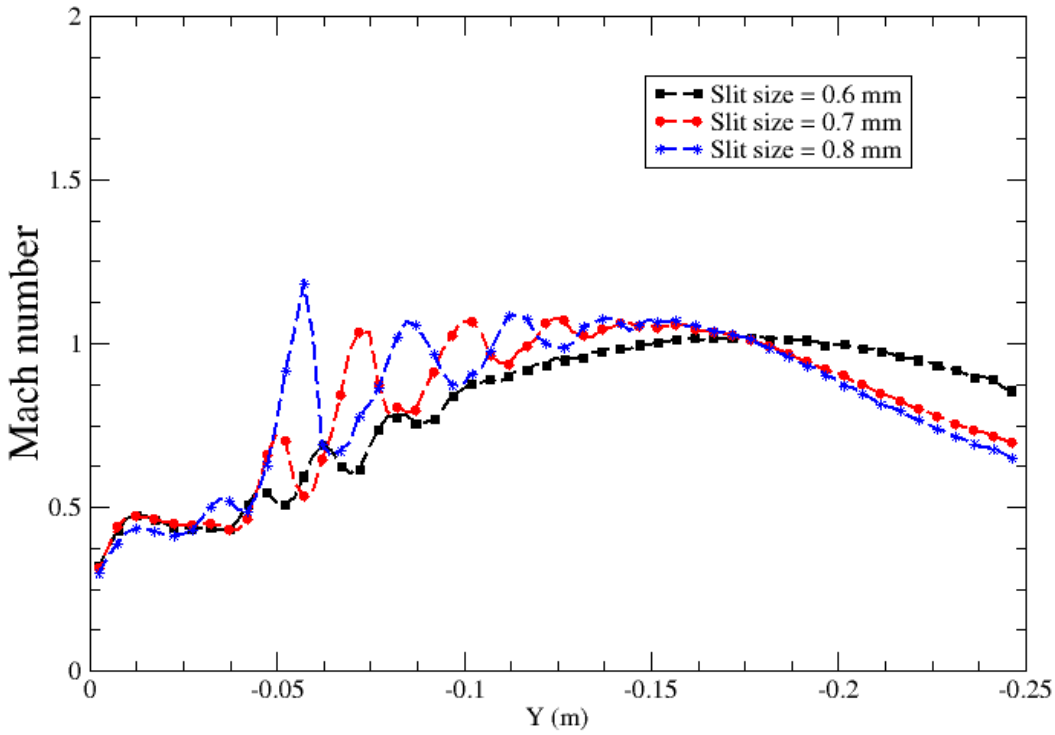

Figure 13 : Evolution of the flow Mach number along the symmetry axis for three different slit sizes. The gas flows from Y= 0 m to Y=-0.25 m.

4.3. Effect of the atomization gas pressure

In this section, the effects on the gas flow of the gas pressure at the nozzle inlets, which is a key operating parameter of the atomization process, are investigated from the simulation results of test cases #1 and #3 in Table 2.

Comparing the gas flow characteristics at the nozzle exit in Tables 3 and 4, it is observed that increasing the inlet pressure from 30 to 45 bar leads to a 34 % increase in the gas pressure and density at the nozzle exit, keeping all other parameters almost identical.

From figures 6 (left) and 11 (middle), one can see that the swirling motion and the gas jet envelope are very little influenced by the increase of the atomization gas pressure. Also, the distributions of the swirl number on the jet envelope are very similar in both cases. On the other hand, there is a strong difference between the Mach number distributions in the atomization tower when the gas pressure is changed from 30 to 45 bar (see figures 7 (right) and 12 (middle)). Increasing the gas pressure causes an important increase of the dimensions of the Mach diamonds (especially their vertical dimension) and enhances the maximum value of the Mach number reached inside each diamond (e.g. the highest value of the Mach number in the first Mach diamond varies from 4.4 for a pressure of 30 bar to 5.1 for a pressure of 45 bar). As a consequence, and as highlighted in Figures 8 (right) and 13 (red dashed-line), the Mach disk associated to the second Mach diamond is shifted significantly downstream (around

25 mm) when the pressure changes from 30 to 45 bar. This trend is similar to what was reported by (Odenthal, et al., 2021) for close coupled system. Moreover, as seen in Figures 8 and 13, the gas flow experiences throughout each compression-expansion waves considerably larger (about 30 % greater) maximum values of the Mach number. The gas flow along the symmetry axis exits definitively the supersonic regime earlier for a lower gas pressure. The location of the corresponding sonic transition is moved 50 mm down when the pressure changes from 30 to 45 bar.

Thus, similarly to the results of previous works on different configurations (Allimant, et al., 2009) (Odenthal, et al., 2021), our modeling results confirm that the inlet gas pressure play a key role on the gas flow characteristics in the atomization tower. Increasing the inlet gas pressure leads to an overall increase in the gas velocity, hence of its kinetic energy, which should be favourable for the liquid metal atomisation and the generation of fine metal powder particles.

4.4. Effect of the gas pressure in the melting chamber

In this section, the effect of various gas overpressure levels in the melting chamber on the swirling supersonic gas flow in the atomization tower is investigated. The results presented correspond to test cases #3, #5 and #6 in Table 2. The nozzle inlet gas pressure is set to 30bar, the gas pressure in the top melting chamber ranges between 1 and 1.6 bar, and the nozzle exit slit size is 0.7 mm.

Figure 14 shows the envelope of the gas flow, defined from the isocontour of the ambient argon density (i.e. 1.76 kg/m^3) and coloured by the swirl number, for three different values of the pressure in the melting chamber. The area and the X and Z dimension ratio of the jet cross-section at the bottom boundary of the computational domain for the three cases are reported in Table 6. Overall, there is a limited influence of the overpressure in the melting chamber on the jet shape and dimensions. The increase of the overpressure reduces slightly the swirling motion of the jet, with an effect being more visible for higher overpressure values. As far as the jet dimensions are concerned, there is little quantitative difference between the pressure of 1 and 1.2 bar. In contrast, the differences become more pronounced when increasing the pressure from 1.2 to 1.6 bar: one observes a widening of the jet in the Z direction and a narrowing in the X direction, which corresponds to a jet becoming less asymmetric.

Figure 15 shows the distribution of the flow Mach number in the XY plane of the atomization tower for the three different pressures in the melting chamber. The effects of the melting chamber pressure on the gas jet are consistent with the observations made in Figure 14. Effects are mainly visible for the higher-pressure values. Yet, they remain moderate. Increasing the pressure from 1.2 to 1.6 bar leads to a slight thinning of the Mach diamonds (more pronounced from the third diamond) and a widening of the inner core of the jet near the nozzle exit, followed by a reduction of the spreading of the jet in the X direction. These latter effects are the sign of a reduced influence of the gas swirling motion with the increase of the pressure in the melting chamber.

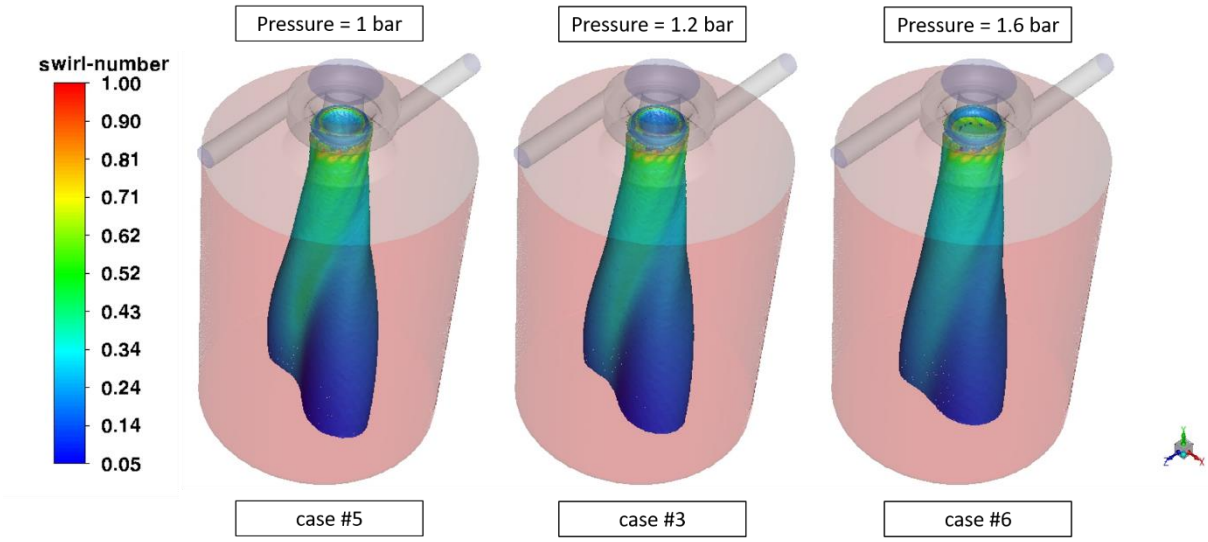

Figure 14 : Visualization of the gas jet envelope coloured by local swirl number for three different pressures in the melting chamber. The envelope is defined from the ambient Ar density isocontour.

Table 6 : Comparison of the area and the X and Z dimension ratio of the jet cross-section at the bottom boundary of the computational domain computed for three melting chamber pressures.

Pressure in the melting chamber (bar)	Surface (mm^2)	Lx / Lz
1 (case #5)	2135	2.98
1.2 (case #3)	2120	2.87
1.6 (case #6)	2097	2.33

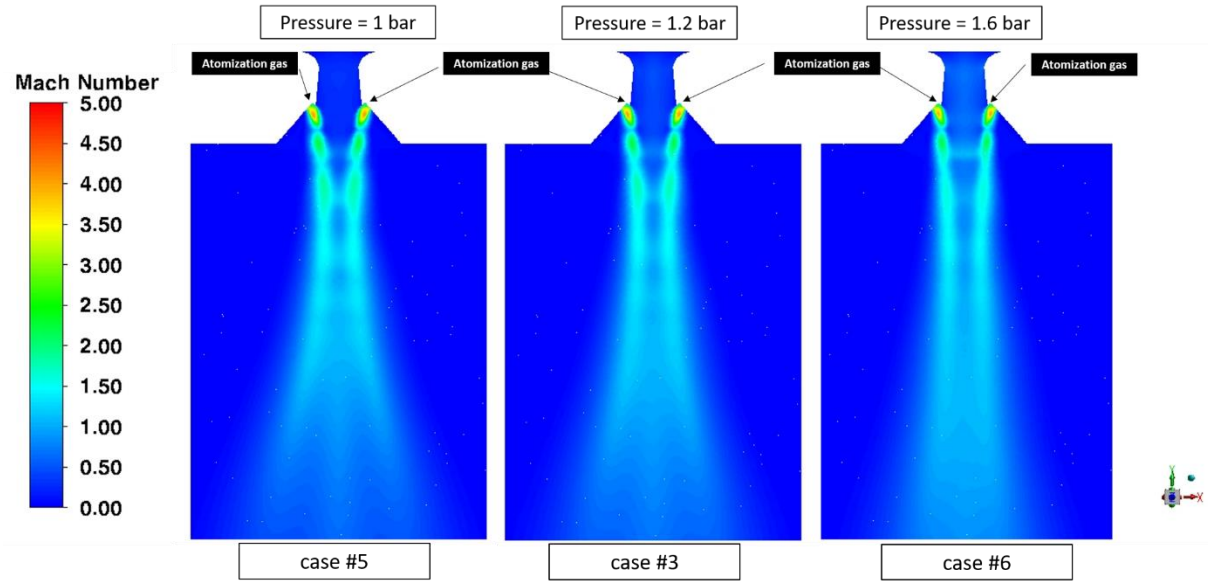

Figure 15 : Distribution of flow Mach number in the XY plane for three different pressures in the melting chamber.

Figure 16 shows the profile of the flow Mach number along the axis of symmetry for the three melting chamber pressures. In the region immediately downstream the melting chamber up to the position Y=-70 mm, it is observed that the Mach number is higher as the pressure is increased. Between Y=-70 mm and Y=-150 mm, the opposite trend occurs, with the Mach number tending to decrease as the pressure is increased. Such an effect is a direct consequence of the less radial spreading of the jet in the X direction induced by the swirling motion as the pressure in the melting chamber is increased. Finally, from the position Y=-150mm the variations of the Mach number reverse back to the same pattern as in the first region close to the nozzle exit. Moreover, the greater the overpressure the further downstream the location of the final sonic transition where the jet flow regime becomes definitively subsonic. The transition is moved 50 mm downstream when the pressure in the melting chamber varies from 1 to 1.6 bar.

Based on the above results, the possible influence of the pressure in the melting chamber on the interactions between the gas and the liquid metal and the metal fragmentation is twofold, with two opposing effects. On one hand, the higher gas flow energy in the region immediately downstream the melting chamber observed for a pressure of 1.6 bar suggests that a high enough pressure in the melting chamber may promote metal fragmentation downstream the melt delivery nozzle thanks to an increased gas velocity. On the other hand, higher pressure levels in the melting chamber are associated to a Mach diamond thinning and widening of the inner core of the jet, which may have a negative influence on the metal fragmentation and favour the generation of large droplets.

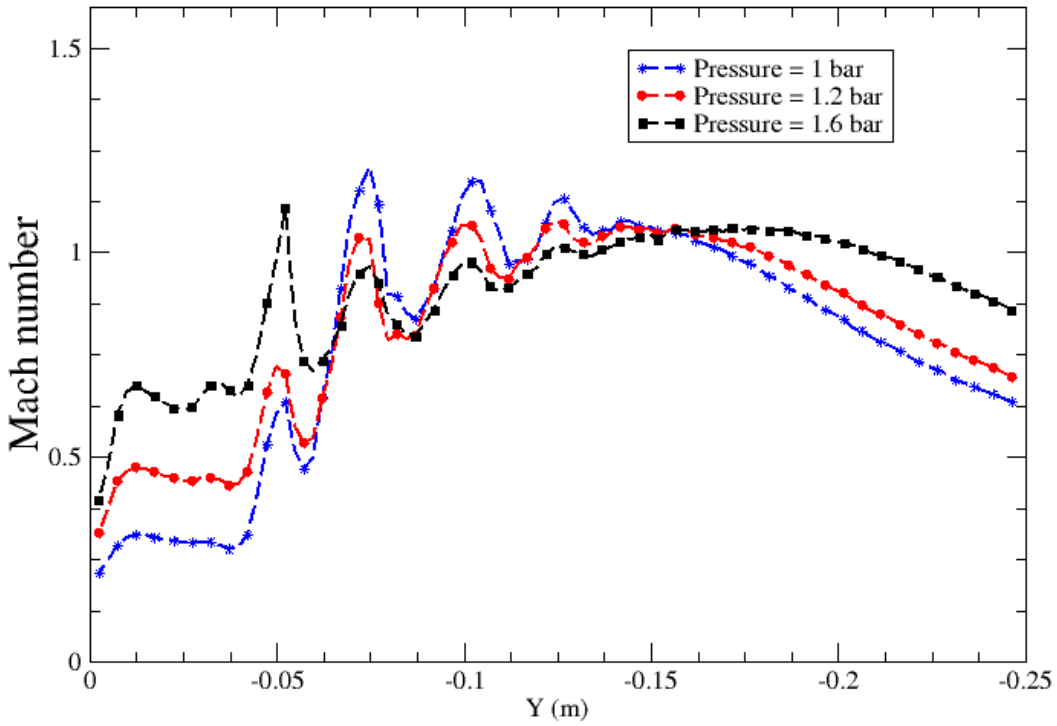

Figure 16 : Evolution of the flow Mach number along the symmetry axis for three different pressures in the melting chamber. The gas flows from Y= 0 m to Y=-0.25 m.

5. Conclusion

A 3D numerical model has been presented to simulate the swirling compressible gas flow through the gas nozzle and inside the atomization chamber of the EIGA process. The developed model is based on the Reynolds-Averaged Navier-Stokes (RANS) approach using the Favre decomposition for compressible flow together with a k-ω SST turbulence model. As part of the present study, the Schlieren imaging technique was also applied to visualize the gas flow patterns downstream of the gas nozzle for validation purposes. The influences of the nozzle exit slit size, the atomization gas pressure and the overpressure between the melting and atomization chambers on the swirling gas flow have been more particularly investigated.

Simulation results revealed that the gas flow regime is kept subsonic through most of the nozzle and turns supersonic just before exiting the nozzle. The gas flow emerging from the nozzle forms a swirling jet with a strongly asymmetric geometry consisting of multiple Mach diamonds. Simulation results regarding the jet horizontal dimension and Mach disk location were in good agreement with the experimental observations from the Schlieren technique.

It was observed that a small increase of the nozzle exit slit size strongly increases the swirl number at the nozzle exit. This leads to a more severe asymmetry of the gas jet in the atomization tower. In addition, increased slit sizes are responsible for larger cellular structures akin to Mach diamonds with higher Mach number values. The maximum value of the Mach number reached in each diamond is increased by about 10 % when the slit size varies from 0.6 to 0.8 mm.

Similarly to the effect of the slit size, it was found that a higher atomization gas pressure makes the jet Mach diamonds and the maximum value of the Mach number reached in each diamond larger. However, in the investigated range (30 to 45 bar), it has a weak influence on the swirling motion and the envelope of the jet.

The influence of the overpressure in the melting chamber remains weak and is mainly visible for high overpressure value. Higher overpressure values induce a moderate increase of the gas flow Mach number near the metal delivery nozzle exit and a reduction of the asymmetry of the jet in the atomization tower.

It has been predicted in this paper that an increase in atomizing gas pressure, an enlargement of the nozzle exit slit size, and a decrease in the overpressure in the melting chamber can result in a finer powder.

In the future, the development of a model describing the fragmentation of the metal stream and the complete atomization process will be addressed completing this first step of development.

Acknowledgements

IRT M2P acknowledges the support of the French “Investissements d’Avenir” Program (ref. ANR-10-AIRT-04) within the framework of the SIGMA project. The authors also thank everyone at MetaFensch and IJL involved in the experimental trials

Bibliography

Allimant A., Planche M.P., Bailly Y., Dembinski L. and Coddet C. Progress in gas atomization of liquid metals by means of a De Laval nozzle. Powder Technology. - 2009. - Vol. 190. - pp. 79–83.

Deborde A. and McDonald N. Atomisation de poudres d'alliages de titane. Traitements & Matériaux. - 2019. - Vol. 458. - pp. 31-36. - In french.

Drawin S., Deborde A., Thomas M., Pierronnet M., Sasaki L., Delfosse J. and Godde O. Atomization of Ti-64 alloy using the EIGA process: comparison of the characteristics of powders produced in labscale and industrial-scale facilities. MATEC Web Conf., The 14th World Conference on Titanium. - 2020. - 07013 : Vol. 321.

Fritsching U. Droplets and particles in sprays: Tailoring particle properties within spray processes. China Particuology. - 2005. - Vol. 3. - pp. 125-133.

Hinze J.O. Turbulence. - New York : McGraw-Hill, 1975.

Hohmann M. and Ludwig N. German patent. - 1991. - DE 4102101 C2.

Huang P. G. , Coleman G. N. and Bradshaw P. Compressible turbulent channel flows: DNS results and modelling. Journal of Fluid Mechanics. - 1995. - pp. 185 - 218.

Hulme-Smith C., Kamalasekaran A. and Sundin S. Simulations of gas flow in gas atomisation of liquid metals and validation experiments. ICLASS 2021, 15th Triennial International Conference on Liquid Atomization and Spray Systems. - 2021.

Kaiser R., Li C., Yang S. and Lee D. A numerical simulation study of the path-resolved breakup behaviors of molten metal in high-pressure gas atomization: With emphasis on the role of shock waves in the gas/molten metal interaction. Advanced Powder Technology. - 2018. - Vol. 29. - pp. 623–630.

Li X. G. and Fritsching U. Process modeling pressure-swirl-gas-atomization for metal powder production. Journal of Materials Processing Technology. - 2017. - Vol. 239 . - pp. 1-17.

Loiseleux T. and Chomaz J.-M. Breaking of rotational symmetry in a swirling jet experiment. Physics of Fluids. - 2003. - Vol. 15.

Luh M. F., Vogl N., Odenthal H. J., Roisman I. V. and Tropea C. Focusing Schlieren Imaging in Close-Coupled Atomization: Comparison of Experimental Results with Numerical Simulations. ICLASS 2018, 14th Triennial International Conference on Liquid Atomization and Spray Systems. - Chicago, USA : [s.n.], 2018.

Menter F. R. Two-equation eddy-viscosity turbulence models for engineering applications. AIAA Journal. - 1994. - 8 : Vol. 32.

Motaman S., Mullis A. M., Cochrane R. F. and Borman D. J. Numerical and Experimental Investigations of the Effect of Melt Delivery Nozzle Design on the Open- to Closed-Wake Transition in Closed-Coupled Gas Atomization. Metallurgical and Materials Transactions B . - 2015. - Vol. 46. - pp. 1990–2004.

Oberleithner K., PASCHEREIT O. and WYGNANSKI I. Vortex Breakdown in a Swirling Jet with Axial Forcing. Congrès Français de Mécanique. - 2007.

Odenthal H. J., Vogl N., Brune T., Apell N., Roisman I. V. and Tropea C. Recent modeling approaches to close-coupled atomization for powder production. In Proceedings of 9th International Conference on Modeling and Simulation of Metallurgical Processes in Steelmaking - STEELSIM2021. - 2021.

Ridolfi M. R. and Folgarait P. Numerical modeling of secondary breakup in molten metals gas-atomization using dimensionless analysis. International Journal of Multiphase Flow. - 2020. - 103431 : Vol. 132.

Rumsey C. L. Compressibility Considerations for k-w Turbulence Models in Hypersonic Boundary-Layer Applications. Journal of Spacecraft and Rockets. - 2010. - Vol. 47(1). - pp. 11-20.

K.P. Rao, S.P. Mehrotra, Effect of process variables on atomization of metals and alloys, Modern Developments in Powder Metallurgy. Metal Powder Industries Federation (MPIF) 1981, pp. 113–130.

Settles G. S. Schlieren and Shadowgraph Techniques - Visualizing Phenomena in Transparent Media. - Berlin, Heidelberg, New York : [s.n.], 2001.

Sun P., Fang Z. Z., Zhang Y. and Xia Y. Review of the Methods for Production of Spherical Ti and Ti Alloy Powder. JOM. - 2017. - Vol. 69. - pp. 1853-1860.

Urionabarrenetxea E., Amatriain A., Avello A. and Martín J. M. Numerical simulation and experimental testing of different close-coupled gas atomiser designs. European Powder Metallurgy Association. - 2021.

Vogl N., Odenthal H. J., Hüllen M., Luh M. F., Roisman I. V. and Tropea C. Physical and numerical modeling of close-coupled atomization processes for metal powder production. METEC & 4th ESTAD -European Steel Technology and Application Days. - 2019.

Wei M. W., Chen S. Y., Liang J. and Liu C. S Effect of atomization pressure on the breakup of TA15 titanium alloy powder prepared by EIGA method for laser 3D printing. Vacuum. - 2017. - Vol. 143. - pp. 185-194.

Yule A.J. and Dunkley J.J. Atomization of Melts for Powder Production and Spray Deposition. Oxford University Press. - 1994.

Zeoli N. and Tabbara H. et Gu S. CFD modeling of primary breakup during metal powder atomization. Chemical Engineering Science. - 2011. - Vol. 66. - pp. 6498-6504.

Zou H. and Xiao Z. Pre-breakup mechanism of free-fall nozzle in electrode induction melting gas atomization. Materials Today Communications. - 2021. - 102778 : Vol. 29.